Increasing the performance of all-solid-state Li batteries by infiltration of Li-ion conducting polymer into LFP-LATP composite cathode

Martin Ihrig[a, ‡,*], Enkhtsetseg Dashjav[a,‡], Alexander M. Laptev [b], Ruijie Ye [a], Daniel Grüner [a], Mirko Ziegner [a], Philipp Odenwald [a], Martin Finsterbusch [a], Frank Tietz [a], Dina Fattakhova-Rohlfing [a,c], Olivier Guillon [a]

[a] *Institute of Energy and Climate Research – Materials Synthesis and Processing, Forschungszentrum Jülich GmbH, 52425 Jülich, Germany*

[b] *Poznan Institute of Technology, 6 Ewarysta Estkowskiego St., 61-755 Poznan, Poland*

[c] *Faculty of Engineering and Center for Nanointegration Duisburg-Essen, University Duisburg-Essen, Lotharstr. 1, 47057 Duisburg, Germany*

[*] Corresponding author

[‡] These authors contributed equally

E-mail address: m.ihrig@fz-juelich.de (M. Ihrig)

Phone: +49-2461-6196841

Fax: +49-2461-619120

Keywords

All-solid-state Li-ion battery; Polymer-ceramic cathode; Tape casting; Free sintering; Enhanced storage capacity; Cycling performance

Highlights

- Free-standing tape-cast LFP-LATP composite cathode.
- Porous tape-cast LFP-LATP scaffold enables its infiltration with polymer electrolyte.
- Polymer infiltration of LFP-LATP cathode ensures nearly complete access of CAM.
- Polymer-LFP-LATP-based cells reveal excellent electrochemical performance.
- Full cells reach an area-specific storage capacity of 3.2 mAh cm-2.

Abstract

Polymer-ceramic composites combine the benefits of polymers and ceramics. In particular, the infiltration of the ceramic cathode with a Li-ion-conducting polymer in an all-solid-state Li battery enhances the utilization of the cathode active material (CAM) and enables the application of thicker cathodes with higher storage capacity. This concept has already been validated in our earlier work, in which a porous $LiCoO_2$-$Li_{6.45}Al_{0.05}La_3Zr_{1.6}Ta_{0.4}O_{12}$ composite cathode was fabricated by spark plasma sintering (SPS). However, its performance stability was low. In the present work, this concept is modified and tape casting and free sintering are used instead of SPS to apply an LFP-LATP cathode with $LiFePO_4$ as CAM, and $Li_{1.5}Al_{0.5}Ti_{1.5}(PO_4)_3$ as the ion-conducting phase . Both tape casting and free sintering are more relevant for large-scale production. The sintered LFP-LATP cathode is infiltrated with the MEEP polymer and $LiC_2NO_4F_6S_2$ ion-conducting salt. A full cell with the polymer-infiltrated cathode, $Li_{6.45}Al_{0.05}La_3Zr_{1.6}Ta_{0.4}O_{12}$ separator, and Li anode shows nearly full LFP utilization in the 100 μm thick cathode with an excellent area-specific storage capacity of above 3 mAh cm^{-2}. However, after a few dozen cycles, a Li dendrite penetrates the separator leading to abrupt capacity fading. The prevention of dendrite formation remains a challenging task for our further work.

1. Introduction

Li-ion batteries are widely used as an energy source in electronic devices and electric vehicles [1,2]. A typical Li-ion battery consists of a solid anode and cathode, liquid or polymer electrolyte, and a separator. The next generation of Li-ion batteries assumes the application of solid electrolytes that can also serve as a separator. These batteries are referred to in the literature as all-solid-state Li batteries (ASSLBs) [1,3]. The advantage of ASSLBs is their fire safety and potentially higher energy storage capacity [1]. An oxide ceramic with perovskite, garnet, or NASICON structure is usually considered a solid electrolyte material [3]. Each of these ceramics has specific advantages and drawbacks concerning ionic conductivity, stability against the anode (e.g., metallic Li), specific weight, cost, etc. [4]. A big challenge in using solid electrolytes is their interaction with the cathode active material (CAM) during sintering and electrochemical cycling with the appearance of low- or non-conductive phases on the interface [4,5]. Only a few CAM-electrolyte combinations show limited interaction at sintering temperatures, e.g., $LiCoO_2$ (LCO) with $Li_{6.45}Al_{0.05}La_3Zr_{1.6}Ta_{0.4}O_{12}$ (LLZO:Al:Ta) [6] and $LiFePO_4$ (LFP) with $Li_{1+x}Al_xTi_{2-x}(PO_4)_3$ (LATP) [7,8]. An important feature of each battery is energy storage capacity. The energy storage capacity can be related to the weight (gravimetric), volume (volumetric), or footprint (areal) of the battery. In particular, the storage capacity of a battery depends on the charge capacity of the CAM. In other words, a CAM should host as many Li-ions per volume as possible. The chemistry of CAM and the design of the cathode are decisive here. In particular, a combination of CAM and electrolyte in a composite cathode results in enhanced CAM utilization in the bulk.

In an earlier publication, we showed an enhanced areal storage capacity for a dense LCO-LLZO:Al:Ta composite cathode [6]. Following this, we achieved even larger storage capacity by infiltration of a porous LCO-LLZO:Al:Ta network with MEEP (poly(bis(2-(2-

mthoxyethoxy)ethoxy)phosphazene) Li-ion conducting polymer [9]. In both cases, we used spark plasma sintering, also known as the field-assisted sintering technique (FAST/SPS), to fabricate the LCO-LLZO:Al:Ta composite cathode. However, FAST/SPS is technically and economically only relevant for small-scale production. Furthermore, the cycling performance of ASSLBs with these cathodes was rather poor with a fast decrease in storage capacity. The low cycling stability of such ASSLBs can be explained by degradation of the LCO/LLZO:Al:Ta interface due to interface amorphization and Co and Al interdiffusion [10].

In the present study, we examine the performance of an alternative LFP-LATP composite cathode infiltrated with MEEP polymer with the aim of improving cycling stability and further increasing storage capacity. LFP is known for its long cycle life and thermal and chemical stability. LFP is environmentally friendly (Co-free) and relatively cheap. However, LFP has a low electronic conductivity [11]. This feature negatively influences the LFP storage capacity. The problem can be solved by adding a carbon phase to the LFP matrix [11]. We generate the carbon phase by pyrolysis of organic binder, as discussed in detail below. The second component of the composite cathode, LATP, is an established solid electrolyte with a NASICON structure. LATP shows good compatibility with LFP, enhanced chemical and thermal stability, and high ionic and low electronic conductivity [7].

Another aim of the current study is to bring the processing route closer to large-scale production. We therefore chose the tape-casting technique, which is widely applied in industry to manufacture thin ceramic sheets [12]. First, the mixture of LFP and LATP powders is dispersed in a slurry holding a dispersant, organic binder, and plasticizer. Then, a raw sheet is formed by flattening the cast slurry. After drying, the LFP-LATP sheet is sintered with evaporation of the solvent, and decomposition of the binder. Binder removal leads to certain porosity in the LFP-

LATP sheet, enabling its infiltration by MEEP polymer. The subsequent electrochemical analysis of the LFP-LATP-MEEP cathode in a LFP-LATP-MEEP|MEEP/LLZO:Al:Ta|Li cell shows nearly full utilization of LFP (CAM) and stable electrochemical cycling. The achieved areal storage capacity is almost 3 times higher than in our previous work [6] and significantly higher than observed for other LFP-containing composite cathodes. However, after 34 cycles, Li dendrite growth through the LLZO:Al:Ta separator leads to a short circuit in the cell. The prevention of Li dendrite formation remains a challenge for our further research.

2. Materials and methods

2.1. Slurry preparation and tape casting

The LATP powder was prepared by solid-state synthesis, as described by Odenwald et al. [13]. The LATP powder was additionally calcined at 700 °C for 4 h. The obtained mean particle size was 0.78 µm, and the specific surface area (BET) was 15.23 m^2 g^{-1}. The commercially available LFP powder (Johnson Matthey) with a mean particle size of 0.5 µm was used without modification. The mixture of LFP and LATP powders (60:40 wt. %) was dispersed in ethanol and methylethylketone solution (34:66 vol. %) with the addition of Nousperse FX9086 (3.5 wt. %) as a dispersant (Elementis), Butvar B-98 (8 wt. %) as a binder (Eastman), PEG 400 and Solusolv 2075 (both 4 wt. %) as plasticizers (Solutia Inc.). All weight contents are related to the weight of LATP. The mixture was homogenized at room temperature within a high-energy planetary mill ARV-310 (Thinky, USA) for 5 minutes at 1500 rpm using 3 to 5 mm ZrO_2 balls (loading of 50:50 wt. %). The organics were polymerized at room temperature for 48 h without rotation. The slurry was degassed at 20 kPa for 10 minutes, and tape cast using a KARO cast 300-7 machine (KARO Electronics Vertriebs GmbH, Germany) with a slit height of 700 µm and a drawing speed of 3 mm s^{-1}. The as-cast LFP-LATP sheet was dried at room temperature for 6 h. The sheet had a thickness of around 140 μm and an in-plane size of around 200 x 200 mm^2 (Fig. 1a). For further characterization, the square samples with a size of 40 x 40 mm^2 were cut off and discs with a diameter of 10, 16, and 18 mm were punched out (Fig. 1b).

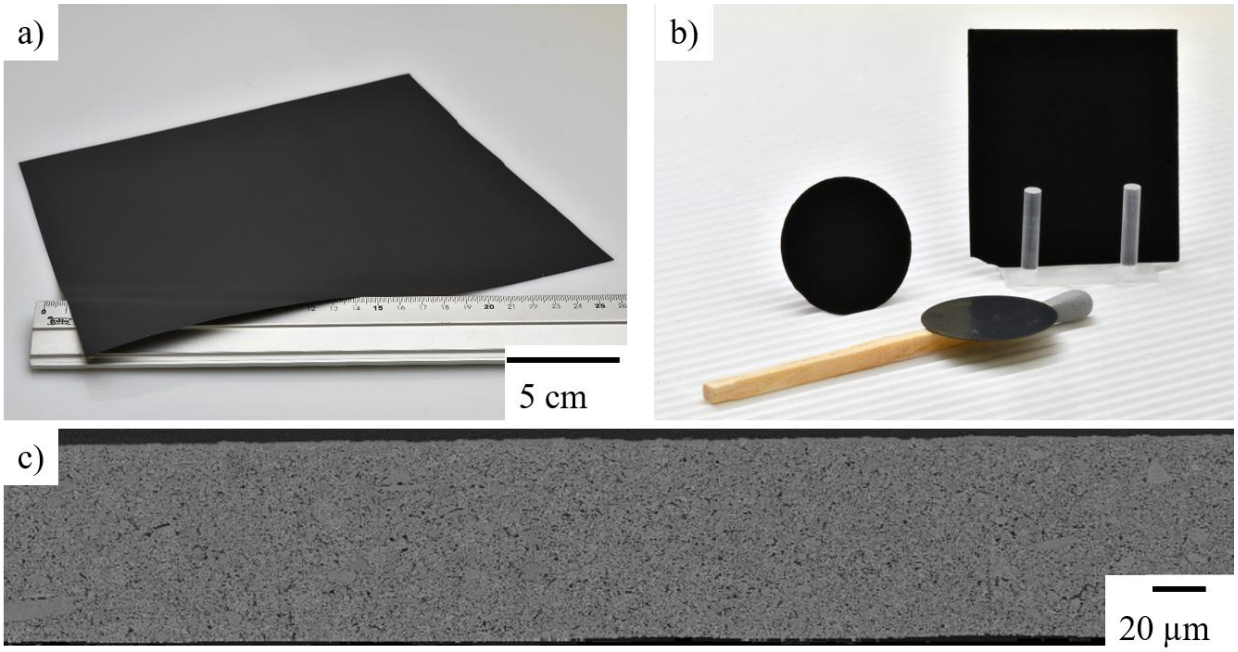

Fig. 1. (a) Tape-cast LFP-LATP sheet before sintering and (b) samples after sintering. (c) Cross-section of sintered LFP-LATP sample.

2.2. Dilatometry, thermogravimetry, and differential thermal analysis

The de-binding and sintering behavior of the tape-cast material was investigated with a 10 mm disc in a push rod dilatometer TMA 402 F1 (Netzsch). The disc was heated to 950 °C with a rate of 5 °C min^{-1} in argon atmosphere. The thermogravimetric analysis (TGA) and differential thermal analysis (DTA) were performed in a STA449F1 Jupiter device (Netzsch). The experiments were conducted with heating up to 800 °C in argon to keep the pyrolyzed carbon as an electrically conducting phase.

2.3. Sintering of tape-cast samples

The LFP-LATP sheets and discs were also sintered in a batch furnace within argon atmosphere. A low heating rate of 1°C min^{-1} was applied up to 500 °C for gentle decomposition of organics followed by a heating rate of 5 °C min^{-1} up to a final sintering temperature of 800 °C. The temperature of 800 °C was maintained for 1 h and then decreased to room temperature at 5 °C min^{-1}. The resulting thickness of the LFP-LATP samples was around 100 μm. The sintering temperature was selected based on the thermal stability analysis for the LFP-LATP composite (see Section 3.1). The application of argon atmosphere during sintering aimed at pyrolysis of organic additives with the formation of free carbon. The free carbon improved the electronic conductivity of the LFP-LATP composite. The sintered LFP-LATP sheets were flat i.e., with no visible warpage or deformation (Fig. 1b). Their microstructure was homogeneous (Fig. 1c). The CAM (LFP) loading related to the footprint of LFP-LATP of the 100 μm thick samples and was around 19.6 mg cm^{-2}.

2.4. Structural characterization

The phase analysis was performed using the X-ray diffraction (XRD) method in the 2θ range from 10° to 80° with a step of 0.02° using a D4 ENDEAVOR (Bruker) diffractometer with Cu-K_α radiation and an LYNXEYE (Bruker) detector. The HighScore software (Malvern Panalytical) and the PDF-2 database (ICDD) were used for phase identification. The Rietveld analysis for refinement of XRD results was conducted using TOPAS 4.2 software (Bruker).

The microstructural characterization was performed on polished cross-sections of samples prepared by Ar ion milling for 7 h with a JEOL SM-09010 polisher. The microstructure was investigated in a MERLIN field emission scanning electron microscope (FE-SEM, Carl Zeiss) with an accelerating voltage of 5 kV. The quantitative image analysis was conducted using Olympus Stream software. The elemental mappings were acquired using the energy-dispersive X-ray spectroscopy (EDX) with an X-max Extreme detector (Oxford Instruments). The data in the maps were refined with the TruMap feature of AZtec software (Oxford Instruments).

2.5. Cell fabrication

The sintered LFP-LATP disks were assembled into full cells, as reported in our earlier paper [11]. After sintering, the porous LFP-LATP sheets were infiltrated by the MEEP Li-ion conducting polymer. The synthesis of MEEP is described in detail by Jankowsky et al. [14]. The infiltrated samples were dried at 80 °C for 1 h and polymerized under UV light for 0.5 h in a UVACUBE 100 chamber (Hönle Group). A thin (approx.10 μm) MEEP polymer layer was used to affix the infiltrated LFP-LATP cathode to the anodic half-cell consisting of a $Li_{6.45}Al_{0.05}La_3Zr_{1.6}Ta_{0.4}O_{12}$ (LLZO:Al:Ta) separator with a mechanically attached Li anode (100 μm in thickness). The synthesis of the LLZO:Al:Ta electrolyte is described by Tsai et al. [15]. The application of the LLZO:Al:Ta separator aimed to inhibit Li dendrite growth towards LATP and prevent short circuits due to MEEP squeezing at anode fixation. The assembled polymer-ceramic cell was placed into an ECC-Std electrochemical tester (El-Cell) and sealed. The structure of the polymer-ceramic LFP-LATP-MEEP|MEEP/LLZO:Al:Ta|Li cell is shown schematically in Fig. 2.

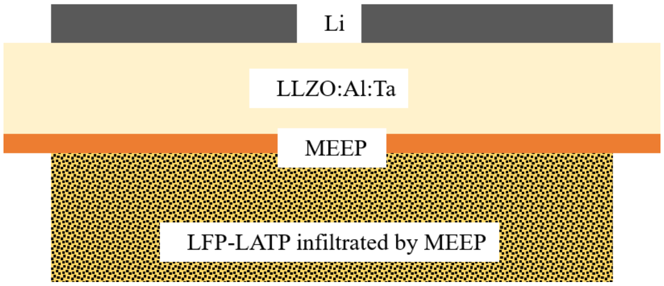

Fig. 2. Schematic view of the full cell.

2.6. Electrochemical characterization

Galvanostatic charge/discharge examination of the polymer-ceramic cells was conducted at 60 °C in a VT 4002EMC (Vötsch) climate chamber using a Maccor potentiostat. The potential window was 2.8–3.9 V vs. Li/Li^+ and the current density was 50 µA cm^{-2}.

3. Results and discussion

3.1. Sintering temperature

The sintering behavior and thermal stability of the LFP-LATP composite were studied using dilatometry and TG/DTA analysis. According to Fig. 3a, the LFP-LATP sample began shrinking at 800 °C. At a temperature of about 910 °C, a kink was visible, followed by abrupt shrinkage. This is a clear indicator of material melting.

The TG graph shows a 15 % weight loss in the temperature range from 100 °C to 550 °C, which is the result of decomposition and pyrolysis of organics (Fig. 3b). This endothermic process is shown in Fig. 3b by a decrease in the DTA signal up to 550 °C. The subsequent increase in the DTA signal (above 600 °C) could indicate a phase transformation in LATP, which was also made visible by XRD.

An exothermic DTA peak recorded at 913 °C (Fig. 3b) is most likely due to a reaction between LFP and LATP with partial melting. This observation correlates with the kink in the shrinkage curve at 910 °C. The results of dilatometry and TG/DTA show that co-sintering of LFP and LATP is possible in a temperature window of 800-900 °C. In the present study, sintering at a temperature of 800 °C was used to achieve open porosity and mechanical stability of the LFP-LATP composite.

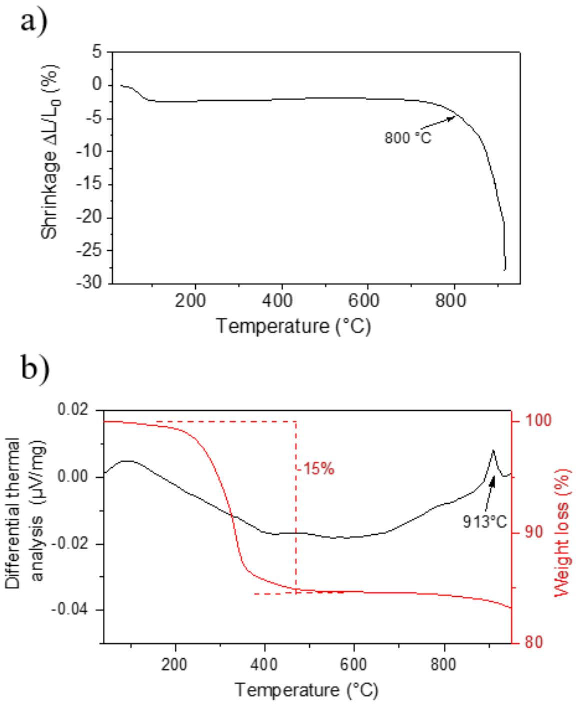

Fig. 3. (a) Dilatometric and (b) TG/DTA diagram for LFP-LATP tape-cast samples.

3.2. Phase analysis

The XRD analysis of the LFP-LATP composite sintered at 800 °C revealed the presence of LFP and LATP phases as well as the formation of a secondary phase, which could not be conclusively identified (Fig. 4). The Rietveld refinement was applied for a more detailed analysis. The refinement with a model mixture of olivine-type LFP (ICSD 15448, [16]), rhombohedral LATP (ICSD 7933, [17]), and $AlPO_4$ (ICSD 98378, [18]) did not describe some of the observed peaks. While the LFP and $AlPO_4$ were well distinguished, the reflections assigned to the rhombohedral LATP were not adequately represented. Therefore, the formation of an orthorhombic structure for LATP was assumed [19]. The result of the Rietveld refinement corresponds to a mixture of 65 wt. % olivine-type LFP (a = 10.326 Å, b = 6.006 Å, c = 4.693 Å), 33 wt. % orthorhombic LATP (a = 8.503 Å, b = 8.573 Å, c = 11.856 Å), and 2 wt. % $AlPO_4$ (a = 7.162 Å, b = 7.077 Å, c = 6.992 Å).

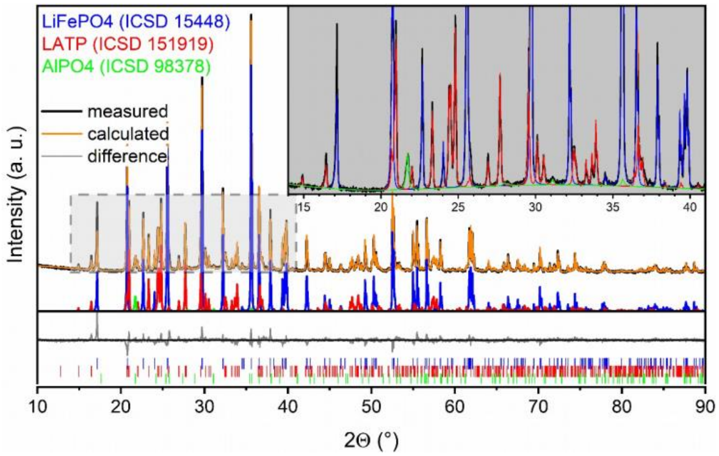

Fig. 4. XRD pattern for sintered LFP-LATP composite and its Rietveld analysis. XRD revealed the olivine-type LFP and orthorhombic LATP as the main phases and $AlPO_4$ as a minor phase. The $AlPO_4$ phase is shown in the inset.

During Rietveld refinement, the atomic positions, site occupation factors, and temperature factors were fixed. The complexity of the diffraction pattern and the presence of different phases in large amounts complicate the verification of possible Al/Fe substitution on the Ti sites or the appearance of a mixed oxidation state for Ti. At the same time, the SEM/EDX analysis did not show the presence of any significant amount of Fe in the orthorhombic LATP (Supplementary material, Fig. S1). Hence, we assume that the composition of LATP remained almost unchanged during the formation of the orthorhombic structure.

3.3. Microstructural analysis

The microstructure of sintered LFP-LATP composite was studied by SEM and EDX spectroscopy. The SEM images revealed a porous structure with a porosity of around 43 % (Figs. 5a and 5b). LFP and LATP were identified as the two main phases based on their contrast and EDX mapping (Figs. 5 and S1). The SEM shows the tight contacts between LFP and LATP particles (Fig. 5). At the same time, the detailed EDX mapping did not reveal any remarkable diffusion across the LFP/LATP interface (Fig. S1). The $AlPO_4$ phase was imaged by SEM as small, isolated grains, forming the Li-ion-blocking areas. This led us to conclude that $AlPO_4$ is unlikely to have a considerable influence on the electrochemical properties of LFP-LATP composite.

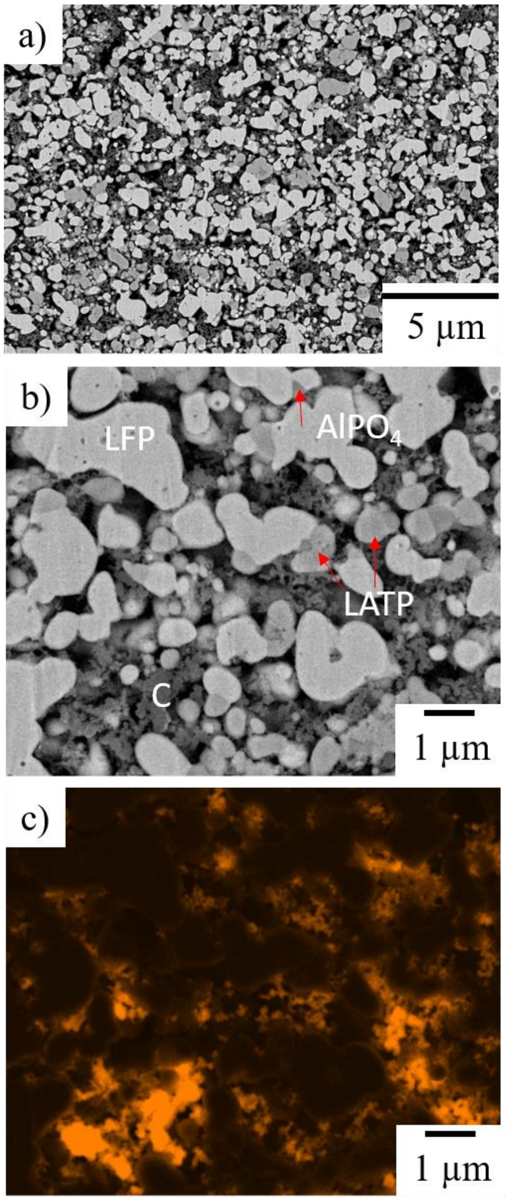

Fig. 5. (a) and (b) SEM images of sintered LFP-LATP composite at two magnifications. LFP, LATP, and $AlPO_4$ phases are distinguished by contrast and labeled in (b). (c) EDX mapping showing the carbon distribution (bright areas) in the LFP-LATP composite.

3.4. Organics pyrolysis and residual carbon

During sintering in argon, the organic components in the tape-cast sheet decomposed with the appearance of carbon particles (Fig. 3b). The EDX mapping in Fig. 5c shows the interconnecting layers of carbon particles. The carbon network increased the electronic conductivity of the LFP-LATP composite, enabling the use of a thicker cathode with enhanced storage capacity.

3.5. Infiltration with MEEP

The open porosity of sintered 100 μm thick LFP-LATP cathode enabled its proper infiltration with MEEP polymer. The EDX mapping for Al and Fe (Fig. 6) shows the homogeneous distribution of LFP and LATP in the composite. The EDX mappings for fluorine (Fig. 6), nitrogen, and sulfur (Fig. S2) show the uniform distribution of MEEP inside the LFP-LATP cathode. The large pores were not entirely filled with polymer. The polymer mainly coated the surface of LFP and LATP particles as a film. Homogeneous MEEP infiltration enables the use of thicker LFP-LATP cathodes with higher areal storage capacity.

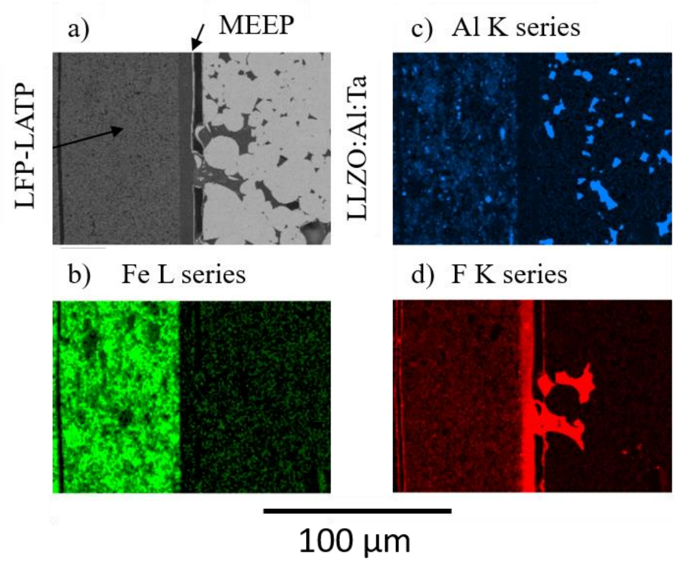

Fig. 6. (a) Overview of cathode/electrolyte interface. (b)-(d) EDX mappings: Fe, Al, and F areas indicate LFP, LATP, and MEEP.

3.6. Electrochemical performance

Fig. 7a shows the charge/discharge curves during cell testing (Fig. 2). In the first charge, the potential firstly increased to 3.9 V (vs. Li/Li$^+$). Then, the gravimetric charge increased at this voltage to a value of around 140 mAh g^{-1}. A large part of the charge in the first cycle occurred at a constant voltage, indicating a high resistance of the investigated cell. The first discharge curve showed a plateau at around 3.35 V (vs. Li/Li$^+$) and a discharge capacity of about 140 mAh g^{-1}. The behavior of the cell continuously improved. All subsequent cycles showed a well-defined charge and discharge plateau at a potential of around 3.25–3.35 V (vs. Li/Li$^+$). The steadily diminished part of the charge at a constant potential indicates a continuous decrease in cell resistance (Fig. 7a). The storage capacity of the cell increased with every charge/discharge cycle, reaching 160 mAh g^{-1} after 10 cycles and 167 mAh g^{-1} after 20 cycles, and remained stable in the subsequent cycles (Fig. 7b). The capacity of 167 mAh g^{-1} corresponds to 98 % of the theoretical capacity of LFP (170 mAh g^{-1}), showing nearly full utilization of the cathode active material. This indicates that the MEEP polymer infiltrated the entire 100 µm thick LFP-LATP cathode and formed a percolating network. In addition, since the LATP completely transformed into an orthorhombic structure, it is plausible that the orthorhombic LATP has electrochemical properties similar to the properties of rhombohedral LATP structure usually reported in the literature [7,8,13,20]. This assumption is in line with the results of Wang et al. and Kee et al. who observed even higher Li-ion diffusivity for the orthorhombic LTP compared to the rhombohedral LTP [21,22].

Due to the nearly full loading of LFP and high thickness of the LFP-LATP cathode, the areal capacity of the cell with the polymer-ceramic cathode was impressively high. A capacity of 3 mAh cm^{-2} was reached after 6 cycles and stabilized at a maximum value of 3.2 mAh cm^{-2} after 20 cycles (Fig. 7b). The areal capacity over 3 mAh cm^{-2} is among the highest results reported for

ASSLBs and is exceeded only by commercially available liquid-electrolyte-based batteries [3,9]. Table 1 demonstrates the excellent electrochemical performance of the considered polymer-infiltrated LFP-LATP cathode in comparison with various ceramic- and polymer-based composite cathodes with LFP as CAM.

In general, the cell with the LFP-LATP cathode infiltrated by MEEP polymer showed continuously increased capacity and stable cycling. However, after 34 cycles, abrupt fading of capacity was observed due to Li dendrite growth through the LLZO:Al:Ta separator, causing the shortcut in the cell. At the same time, we did not observe (at least by SEM) any mechanical or material degradation in the cycled cell (Fig. S3). In summary, the presented results show the high potential of ASSLBs with a tape-cast LFP-LATP composite cathode infiltrated by MEEP polymer. The ASSLBs of this type reveal nearly full CAM utilization even for a relatively thick cathode, excellent areal capacity, and good cycling stability. However, the prevention of Li dendrite formation remains a challenging task.

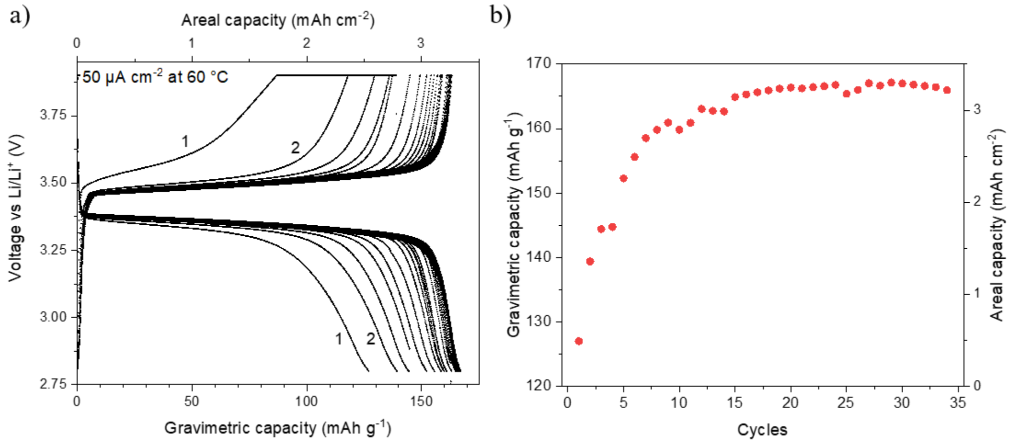

Fig. 7. (a) Cycling performance of cell with LFP-LATP cathode infiltrated by MEEP. (b) Gravimetric and areal storage capacity of LFP in LFP-LATP cathode infiltrated by MEEP.

Table 1. LFP loading and storage capacity of composite cathodes in the literature and the present paper

Cathode	LFP loading, mg cm^{-2}	Current dens., µA cm^{-2}	Cycles	Temperature, °C	Storage capacity, mAh g^{-1}	mAh cm^{-2}	Ref.
LFP-PVdF	1.2	10	100	60	150	0.18	[23]
LFP-PEO	~5	170	100	65	130	0.65	[24]
LFP-PEO	3-5	100	50	60	140	0.42-0.70	[25]
LFP-PEO	3.3	185	210	60	155	0.53	[26]
LFP-C-PVdF	2.5	8	5	25	148	0.37	[27]
LFP-LATP-MEEP	**19.6**	**50**	**34**	**60**	**165**	**3.2**	**This work**

4. Conclusions

The tape-casting technology was successfully used to fabricate LFP-LATP (60:40 wt. %) composite cathodes. The sintering window for the LFP-LATP composite was 800-900 °C. Sintering in argon atmosphere resulted in the pyrolysis of organics with the appearance of carbon nanoparticles. The pyrolyzed carbon was deposited mainly on the surface of LFP and LATP particles. The carbon network enhanced the electronic conductivity of the LFP-LATP composite. The decomposition of organics during the sintering of the LFP-LATP tape-cast sheet resulted in an open porosity of about 43%. This porosity was sufficient for the infiltration and percolation of the LFP-LATP network by the Li-ion conducting MEEP polymer. The enhanced ionic conductivity of the composite cathode achieved with LATP and MEEP phases enabled nearly full utilization of the active material (LFP), even in cathodes with a high thickness (in this work 100 μm). The nearly full CAM loading in combination with a high cathode thickness ensured a high area-specific storage capacity (in this work more than 3 mAh cm^{-2}). In addition, a representative cell with the polymer-infiltrated cathode showed stable cycling (34 cycles in this work) until the formation of a Li dendrite. The increase in the electrochemical performance must be addressed in future work. This includes increased areal capacity for thicker cathodes, high-voltage CAMs, and higher cycling stability by preventing the formation of Li dendrites.

Credit authorship contribution statement

Martin Ihrig: Conceptualization, Writing – original draft, Data curation **Enkhtsetseg Dashjav:** Methodology, Investigation, Validation. **Alexander M. Laptev:** Writing – original draft, Writing – review & editing. **Rainie Ye:** Writing – review & editing. **Daniel Griner:** Investigation, Methodology. **Mirko Zeiger:** Investigation, Methodology. **Philipp Dewald:** Methodology. **Martin Instruct:** Project administration. **Frank Dietz:** Supervision. **Dina Fattakhova-Rohlfing:** Project administration. **Olivier Guillon:** Acquisition of funding.

Declaration of competing interest

The authors declare that they have no known competing financial interests or personal relationships that could have appeared to influence the work reported in this paper.

Acknowledgments

This work was financially supported by the German Federal Ministry of Education and Research (grant numbers: 13XP0184B, 13XP0228D, and 13XP0305A). The authors are thankful to M.T. Gerhards for dilatometry and DTA/TGA experiments and to H.-D. Wiemhöfer for providing the MEEP polymer. The authors take full responsibility for the content of this publication.

Appendix A. Supplementary material

Supplementary material to this article can be found online at

References

[1] Y. Xiao, Y. Wang, S.-H. Bo, J.C. Kim, L.J. Miara, G. Ceder, Understanding interface stability in solid-state batteries, Nat. Rev. Mater. 5 (2020) 105-126. https://doi.org/10.1038/s41578-019-0157-5.

[2] J.M. Tarascon, M. Armand, Issues and challenges facing rechargeable lithium batteries, Nature 414 (2001) 359-367. https://doi.org/10.1038/35104644.

[3] J. Janek, W.G. Zeier, 2016. A solid future for battery development. Nat. Energy 1, 16141. https://doi.org/10.1038/nenergy.2016.141

[4] A. Manthiram, X. Yu, S. Wang, 2017. Lithium battery chemistries enabled by solid-state electrolytes, Nat. Rev. Mater. 2, 16103. https://doi.org/10.1038/natrevmats.2016.103.

[5] L. Miara, A. Windmuller, C.L. Tsai, W.D. Richards, Q.L. Ma, S. Uhlenbruck, O. Guillon, G. Ceder, About the compatibility between high voltage spinel cathode materials and solid oxide electrolytes as a function of temperature, ACS Appl. Mater. Interfaces 8 (2016) 26842-26850. https://doi.org/10.1021/acsami.6b09059.

[6] M. Ihrig, M. Finsterbusch, C.-L. Tsai, A.M. Laptev, C.-h. Tu, M. Bram, Y.J. Sohn, R. Ye, S. Sevinc, S.-k. Lin, D. Fattakhova-Rohlfing, O. Guillon, 2021. Low-temperature sintering of fully inorganic all-solid-state batteries. – Impact of interfaces on full cell performance. J. Power Sources 482, 228905. https://doi.org/10.1016/j.jpowsour.2020.228905.

[7] M. Gellert, E. Dashjav, D. Grüner, Q. Ma, F. Tietz, Compatibility study of oxide and olivine cathode materials with lithium aluminum titanium phosphate, Ionics 24 (2018) 1001-1006. https://doi.org/10.1007/s11581-017-2276-6.

[8] E. Dashjav, M. Gellert, G. Yan, D. Grüner, N. Kaiser, S. Spannenberger, I. Kraleva, R. Bermejo, M.-T. Gerhards, Q. Ma, J. Malzbender, B. Roling, F. Tietz, O. Guillon, Microstructure, ionic conductivity, and mechanical properties of tape-cast $Li_{1.5}Al_{0.5}Ti_{1.5}P_3O_{12}$ electrolyte sheets, J. Eur. Ceram. Soc. 40 (2020) 1975-1982. https://doi.org/10.1016/j.jeurceramsoc.2020.01.017.

[9] M. Ihrig, R. Ye, A.M. Laptev, D. Grüner, R. Guerdelli, W.S. Scheld, M. Finsterbusch, H.-D. Wiemhöfer, D. Fattakhova-Rohlfing, O. Guillon, Polymer–ceramic composite cathode with enhanced storage capacity manufactured by field-assisted sintering and infiltration, ACS Appl. Energy Mater. 4 (2021) 10428-10432. https://doi.org/10.1021/acsaem.1c02667.

[10] M. Ihrig, M. Finsterbusch, A.M. Laptev, C.-H. Tu, N.T.T. Tran, C.-A. Lin, L.-Y. Kuo, R. Ye, Y.J. Sohn, P. Kaghazchi, S.-K. Lin, D. Fattakhova-Rohlfing, O. Guillon, Study of $LiCoO_2/Li_7La_3Zr_2O_{12}$:Ta interface degradation in all-solid-state lithium batteries, ACS Appl. Mater. Interfaces 14 (2022) 11288-11299, https://doi.org/10.1021/acsami.1c22246.

[11] L.-X. Yuan, Z.-H. Wang, W.-X. Zhang, X.-L. Hu, J.-T. Chen, Y.-H. Huang, J.B. Goodenough, Development and challenges of $LiFePO_4$ cathode material for lithium-ion batteries, Energy Environ. Sci. 4 (2011) 269-284. https://doi.org/10.1039/C0EE00029A.

[12] L. Ren, X. Luo, H. Zhou, The tape casting process for manufacturing low-temperature co-fired ceramic green sheets: A review, J. Am. Ceram. Soc. 101 (2018) 3874-3889. https://doi.org/10.1111/jace.15694.

[13] P. Odenwald, Q. Ma, B. Davaasuren, E. Dashjav, F. Tietz, M. Wolff, W. Rheinheimer, S. Uhlenbruck, O. Guillon, D. Fattakhova-Rohlfing, 2021. The impact of lithium tungstate on the densification and conductivity of phosphate lithium-ion conductors. ChemElectroChem 9, e202101366. https://doi.org/https://doi.org/10.1002/celc.202101366.

[14] S. Jankowsky, M.M. Hiller, R. Stolina, H.D. Wiemhöfer, Performance of polyphosphazene based gel polymer electrolytes in combination with lithium metal anodes, J. Power Sources 273 (2015) 574-579. https://doi.org/10.1016/j.jpowsour.2014.09.077.

[15] C.-L. Tsai, E. Dashjav, E.-M. Hammer, M. Finsterbusch, F. Tietz, S. Uhlenbruck, H.P. Buchkremer, High conductivity of mixed phase Al-substituted $Li_7La_3Zr_2O_{12}$, J. Electroceram. 35 (2015) 25-32. https://doi.org/10.1007/s10832-015-9988-7.

[16] T. Yoshinari, T. Mori, K. Otani, T. Munesada, K. Yamamoto, T. Uchiyama, K. Fukuda, Y. Koyama, R. Hagiwara, Y. Orikasa, Y. Uchimoto, Quantitative elucidation of the non-equilibrium phase transition in $LiFePO_4$ via the intermediate phase, Chem. Mater. 31 (2019) 7160-7166. https://doi.org/10.1021/acs.chemmater.9b00834.

[17] G.J. Redhammer, D. Rettenwander, S. Pristat, E. Dashjav, C.M.N. Kumar, D. Topa, F. Tietz, A single-crystal X-ray, and powder neutron diffraction study on NASICON-type $Li_{1+x}Al_xTi_{2-x}(PO_4)_3$ $(0 \leq x \leq 0.5)$ crystals: Implications on ionic conductivity, Solid State Sci. 60 (2016) 99-107. https://doi.org/10.1016/j.solidstatesciences.2016.08.011.

[18] H.A. Graetsch, Thermal expansion and thermally induced variations of the crystal structure of $AlPO_4$ low cristobalite, Neues Jahrb. für Mineral. Monatshefte 7 (2003) 289-301. https://doi.org/10.1127/0028-3649/2003/2003-0289

[19] M. Catti, A mixed α/β superstructure in NASICON ionic conductors: neutron diffraction study of $Li_2FeTi(PO_4)_3$ and $Li_2FeZr(PO_4)_3$, J. Solid State Chem. 156 (2001) 305-312. https://doi.org/10.1006/jssc.2000.8999.

[20] J.P. Gross, J. Malzbender, E. Dashjav, F. Tietz, R. Schwaiger, Conductivity, microstructure and mechanical properties of tape-cast LATP with LiF and SiO_2 additives, J. Mater. Sci. 57 (2022) 925-938. https://doi.org/10.1007/s10853-021-06773-6.

[21] S. Wang, S.-J. Hwu, A new mixed valent titanium (III/IV) phosphate with a NASICON-type structure, J. Solid State Chem., 90 (1991) 377-381. https://doi.org/10.1016/0022-4596(91)90156-C.

[22] Y. Kee, S.-S. Lee, H. Yun, 2011. The mixed-valent titanium phosphate, $Li_2Ti_2(PO_4)_3$, dilithium dititanium(III/IV) tris(orthophosphate), Acta Crystallogr., E 67, i49. https://doi.org/doi:10.1107/S1600536811031606.

[23] F. Du, N. Zhao, Y. Li, C. Chen, Z. Liu, X. Guo, All-solid-state lithium batteries based on lamellar garnet-type ceramic electrolytes, J. Power Sources, 300 (2015) 24-28. https://doi.org/10.1016/j.jpowsour.2015.09.061.

[24] W. Zhou, S. Wang, Y. Li, S. Xin, A. Manthiram, J.B. Goodenough, Plating a dendrite-free lithium anode with a polymer/ceramic/polymer sandwich electrolyte, J. Am. Chem. Soc., 138 (2016) 9385-9388. https://doi.org/10.1021/jacs.6b05341.

[25] Q. Zhou, B. Xu, P.-H. Chien, Y. Li, B. Huang, N. Wu, H. Xu, N.S. Grundish, Y.-Y. Hu, J.B. Goodenough, 2020. NASICON $Li_{1.2}Mg_{0.1}Zr_{1.9}(PO_4)_3$ solid electrolyte for an all-solid-state li-metal battery, Small Methods, 4, 2000764. https://doi.org/10.1002/smtd.202000764.

[26] X. Yang, M. Jiang, X. Gao, D. Bao, Q. Sun, N. Holmes, H. Duan, S. Mukherjee, K. Adair, C. Zhao, J. Liang, W. Li, J. Li, Y. Liu, H. Huang, L. Zhang, S. Lu, Q. Lu, R. Li, C.V. Singh, X. Sun, Determining the limiting factor of the electrochemical stability window for PEO-based solid polymer electrolytes: main chain or terminal –OH group? Energy Environ. Sci., 13 (2020) 1318-1325. http://dx.doi.org/10.1039/D0EE00342E.

[27] S.A. Pervez, G. Kim, B.P. Vinayan, M.A. Cambaz, M. Kuenzel, M. Hekmatfar, M. Fichtner, S. Passerini, 2020. Overcoming the interfacial limitations imposed by the solid-solid interface in

solid-state batteries using ionic liquid-based interlayers, Small, 16, 2000279. https://doi.org/10.1002/smll.202000279.